Foam-driven fracture

Ching-Yao Lai[a], Bhargav Rallabandi[a], Antonio Perazzo[a], Zhong Zheng[b], Samuel E. Smiddy[c], and Howard A. Stone[a,1]

[a]Department of Mechanical and Aerospace Engineering, Princeton University, Princeton, NJ 08544; [b]BP Institute, University of Cambridge, Cambridge CB3 0EZ, United Kingdom; and [c]Department of Chemical and Biological Engineering, Princeton University, Princeton, NJ 08544

Edited by David A. Weitz, Harvard University, Cambridge, MA, and approved July 5, 2018 (received for review May 14, 2018)

In hydraulic fracturing, water is injected at high pressure to crack shale formations. More sustainable techniques use aqueous foams as injection fluids to reduce the water use and wastewater treatment of conventional hydrofractures. However, the physical mechanism of foam fracturing remains poorly understood, and this lack of understanding extends to other applications of compressible foams such as fire-fighting, energy storage, and enhanced oil recovery. Here we show that the injection of foam is much different from the injection of incompressible fluids and results in striking dynamics of fracture propagation that are tied to the compressibility of the foam. An understanding of bubble-scale dynamics is used to develop a model for macroscopic, compressible flow of the foam, from which a scaling law for the fracture length as a function of time is identified and exhibits excellent agreement with our experimental results.

hydraulic fracturing | fluid–structure interactions | foams | fluid-driven cracks | foam fracturing

The flow of compressible aqueous foam has a broad range of applications, such as fire-fighting (1–3), compressed air energy storage (4), materials processing (5), and enhanced oil recovery, where the injection of foam instead of water (6–12) suppresses viscous fingering at the fluid–fluid interface. In hydraulic fracturing (13, 14), water is injected at high pressure to crack shale formations, releasing trapped oil and natural gas. Alternative techniques using foams as injection fluids have been developed to reduce the water use of conventional hydrofracture (15–17). Here we show that when a foam is injected at high pressures to fracture an elastic medium, the foam compressibility produces a time-dependent flow that controls the dynamics of fracture propagation.

Although steady flow of foam in pipes (3, 10, 18–22) and 2D channels (6, 23) has been studied extensively, time-dependent foam flows resulting from the compressibility of bubbles are poorly understood. Here, we quantify these unsteady flows using one-dimensional model experiments, which we rationalize using mechanical principles. Using these results, we develop scaling relations for the propagation of foam-driven brittle fractures that are in quantitative agreement with our experiments.

A Qualitative Observation for Foam-driven Fractures

We fracture an elastic solid matrix by injecting into it an aqueous foam from a syringe, through a tube and needle (Fig. 1*A*). The elastic matrix is chosen to be gelatin since it models the brittle and elastic properties of rocks (24–29) and allows us to visualize the fracture dynamics (24, 26, 27, 30–32). We use Gillette® Foamy shaving foam in our experiments due to its well-known and robust properties (33–36). Initially, the syringe, tube, and needle are filled with foam that is at equilibrium with atmospheric pressure p_∞. During the experiment, the volume of the syringe decreases with time at a rate Q. Initially, the injection causes the foam in the entire system to be compressed. Once the foam in the syringe reaches a certain volumetric strain ($\approx$ 30% for the experiment shown in Fig. 1 *C* and *D*), the foam fractures the elastic matrix in a lens shape (37) [also referred to as a penny shape (38)] and propagates along a plane (Fig. 1 *C* and *D*). We are interested in the growth of the crack radius $R(t)$ for a constant volumetric rate of injection Q. For an incompressible flow, the volume of the crack V grows as Qt. However, we find that the dynamics of the crack growth are altered by the compressibility of the foam, as we discuss below.

The pressure drop along the tube and needle can be estimated from a balance of stresses in the foam. The pressure gradient along the foam flow balances the shear stress gradient across the tube; the inertia of the foam is negligible for the injection rates studied here. Therefore, the shear stress at the tube wall is $\tau_w = -\frac{a}{2}\frac{\partial p}{\partial z}$, where z is in the flow direction and a is the tube radius. For smooth walls and τ_w smaller than the yield stress, the foam moves as a plug with velocity u, lubricated by a thin film of liquid with viscosity μ near the wall (39). Denkov et al. (39) showed that $\tau_w \approx \kappa(\mu\gamma u)^{1/2}/(2\bar{R})$, where γ is the interfacial tension and $\bar{R}$ is the mean radius of the bubbles (40). Here, κ is a dimensionless resistance that depends on the liquid volume fraction ϵ of the foam and is related to the fractional area of the tube wall wetted by liquid films (39, 41, 42) (see *SI Appendix*). Combining these approximations, the average velocity of foam in the tube of length ℓ obeys

$$u = u_D\left(\frac{\partial(p/p_\infty)}{\partial(z/\ell)}\right)^2, \quad \text{where} \quad u_D = \frac{(\bar{R}ap_\infty)^2}{\gamma\mu(\kappa\ell)^2} \qquad [1]$$

is the typical foam velocity when the pressure drop along the tube is on the order of atmospheric pressure p_∞—that is, $\partial(p/p_\infty)/\partial(z/\ell) = \mathcal{O}(1)$. Relative motion between liquid and

Significance

Hydraulic fracturing plays an important role in meeting today's energy demands. However, the substantial use of fresh water in fracturing and wastewater returning to the surface pose risks to the environment. Alternative technology has been developed that reduces the water-related risks by injecting aqueous foam instead of water to fracture shale formations, but the mechanism is poorly understood. Here, we show, using laboratory experiments, that the injection of foam instead of water dramatically changes the fracture dynamics when the foam compressibility is important. We develop a scaling argument for the fracture dynamics that exhibits excellent agreement with the experimental results. Our findings extend to other systems involving compressible foams, including fire-fighting, energy storage using compressed foams, and enhanced oil recovery.

Author contributions: C.-Y.L., B.R., A.P., and H.A.S. designed research; C.-Y.L., B.R., S.E.S., and H.A.S. performed research; C.-Y.L., B.R., A.P., Z.Z., and H.A.S. contributed analytic tools; C.-Y.L., B.R., A.P., S.E.S., and H.A.S. analyzed data; and C.-Y.L., B.R., A.P., and H.A.S. wrote the paper.

The authors declare no conflict of interest.

This article is a PNAS Direct Submission.

[1]To whom correspondence should be addressed. Email: hastone@princeton.edu.

This article contains supporting information online at www.pnas.org/lookup/suppl/doi:10.1073/pnas.1808068115/-/DCSupplemental.

Published online July 26, 2018.

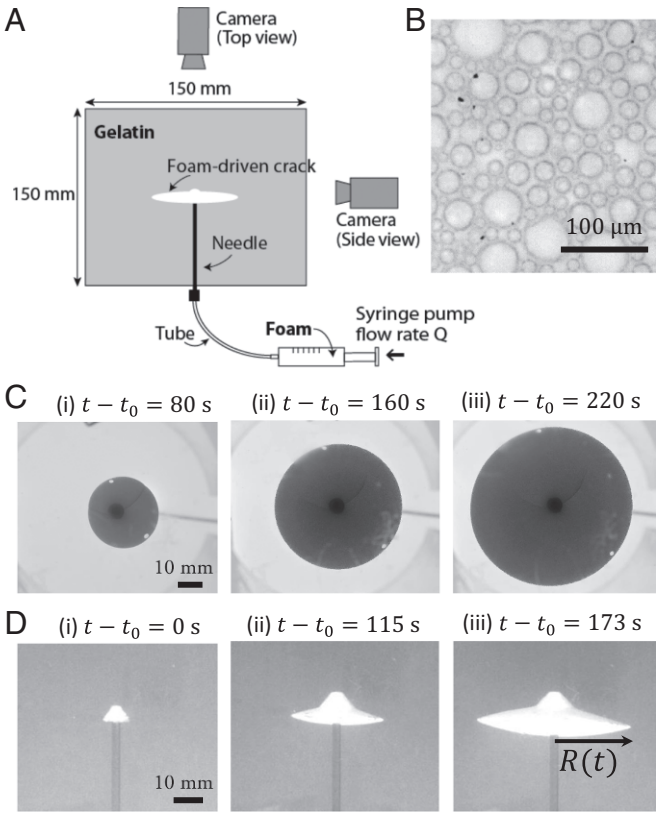

Fig. 1. (*A*) Schematic of the experimental setup. Foam is injected from a syringe (initial volume $V_0 = 25$ mL) through a tube (radius, 0.89 mm; length, 0.32 m; initial volume, 0.8 mL) and needle (radius, 1.08 mm; length, 0.11 m; initial volume, 0.4 mL) into an elastic gelatin matrix. (*B*) A microscopic view of the foam (Gillette® Foamy), whose constituents include water and hydrocarbon gases. The bubble radii range from 6 to 47 μm (polydisperse). The growth of a lens-shaped crack driven by foam injection is observed from both (*C*) top and (*D*) side. In this experiment, $t_0 = 40$ s, where t_0 denotes the time at which foam first enters the elastic matrix.

bubbles [i.e., drainage (43–45)] is negligible for the pressure gradients used in our experiments.

To estimate the pressure drop along the tube, we measured the liquid properties, $\gamma = 29 \pm 2$ mN/m and $\mu = 3 \pm 1$ mPa·s, after separating the liquid phase using a centrifuge (see *SI Appendix*). We measured the mean bubble radius $\bar{R} = 12 \pm 1$ μm using optical microscopy (e.g., Fig. 1*B*). We weighed the foam at p_∞ to determine its liquid volume fraction $\epsilon_\infty \approx 0.1$, and note that $\kappa(\epsilon = \epsilon_\infty) \approx 4$ (see *SI Appendix*). For a typical measured foam velocity in the tube $u \approx 1.5$ cm/s, we estimate using Eq. **1** that the typical pressure drop along the injection tube is $\Delta p_t \approx (\gamma\mu u)^{1/2}\kappa\ell/(\bar{R}a) \approx 1.8 \times 10^5$ Pa. We measured the foam pressure during the fracturing experiment and also found the typical foam pressure drop along the tube to be $\mathcal{O}(10^5)$ Pa (see *SI Appendix*). Since $\Delta p_t = \mathcal{O}(p_\infty)$, compressibility effects are important. The foam does not coarsen significantly for the range of pressures in our experiments (see *SI Appendix*).

When a foam-driven fracture of a typical radius $R \approx 20$ mm and thickness $2W \approx 8$ mm is generated in the gelatin matrix (Young's modulus $E \approx 66$ kPa, Poisson's ratio $\sigma \approx 0.5$), the typical elastic stress due to the elastic deformation around the fracture is $\Delta p_e \approx EW/(2(1-\sigma^2)R) \approx 8.8 \times 10^3$ Pa (37, 46, 47). Since $\Delta p_t \gg \Delta p_e$, the stresses related to fracture formation are negligible compared with the pressure drop in the foam along the tube. Therefore, to better understand the dynamics, the foam flow can be modeled with a one-dimensional experiment where a tube of length ℓ and radius a is connected to a syringe. The outlet of the tube, rather than connecting to an elastic matrix, is directly exposed to atmospheric pressure (Fig. 2*A*). Note that ℓ represents the combined length of the tube and needle in the fracture experiments (Fig. 1*A*).

A One-Dimensional Model Experiment

In the one-dimensional model experiment (Fig. 2*A*), the entire tube and the syringe are filled with foam at atmospheric pressure, and the syringe is compressed at a volumetric rate Q (see Table 1). As with the fracture experiment, no foam flow is observed at the tube outlet until time t_0. To characterize the flow, we measure the volume of foam collected at the outlet of the tube as a function of time $V(t)$ (Fig. 2*B*). The experiment ends when the foam in the syringe is completely injected into the tube. Experimental parameters are summarized in Table 1.

For incompressible flows, mass conservation necessitates that $V(t) = Q(t - t_0)$ (see experiment K and the dashed line in Fig. 2*B*). However, in the foam experiments (experiments A–J), we

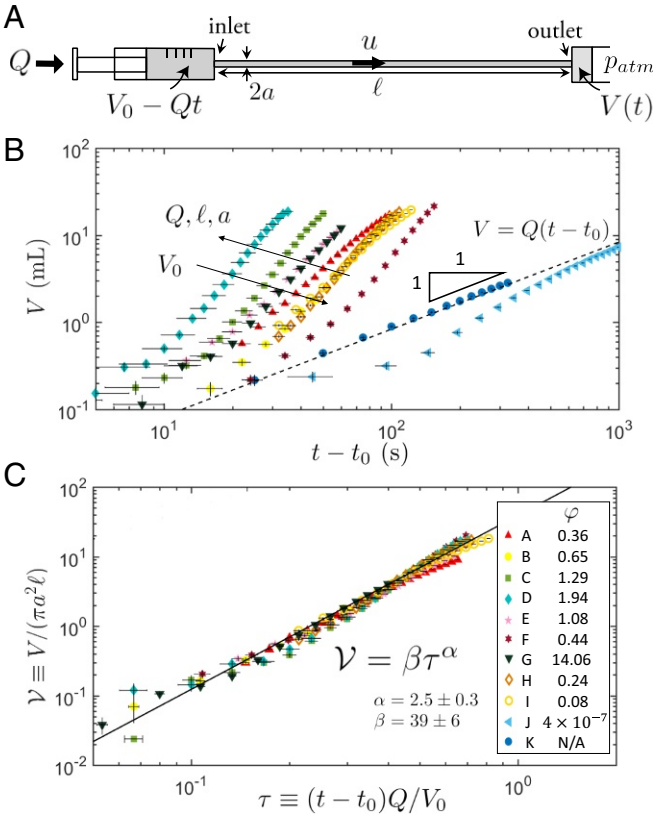

Fig. 2. (*A*) Foam flow in a tube of length ℓ and radius *a*. The tube inlet connects to a syringe filled with foam (volume V_0), and the tube outlet is exposed to atmospheric pressure. The syringe pump reduces the syringe volume with a constant injection rate *Q*. Initially no foam is observed to exit the outlet of the tube, and the foam in the entire system is compressed. At t_0, foam exits the tube outlet. (*B*) The volume of foam collected at the outlet of the tube *V* is measured as a function of time for different *Q*, ℓ, *a*, V_0, μ, and ϵ_∞. The experimental parameters are shown in Table 1. Two flow regimes are observed. When $\varphi \ll 1$ (Expt. J), where φ is defined in Eq. **2**, *V* approaches the steady-state incompressible results, $V = Q(t - t_0)$, as shown by the dashed line. When $\varphi = \mathcal{O}(1)$, foam compressibility affects the flow and a nonlinear dependence of *V* on *t* is observed (experiments A–I). (*C*) The dimensionless volume $\mathcal{V}$ versus dimensionless time τ for the fast-injection experiments (experiments A–I) collapses onto a universal curve. For simplicity, we fit a power-law function to the dimensionless curve $\mathcal{V}(\tau)$, as shown by the solid line (Eq. **3**).

Table 1. Experimental parameters for the one-dimensional model experiments (experiments A–K) shown in Fig. 2

Experiment	Q, mL/min	ℓ, m	a, mm	V_0, mL	μ, mPa· s	ϵ_∞	Fluid
A	10	0.43	1.19	25	3	0.1	Foam
B	10	0.43	0.89	25	3	0.1	Foam
C	20	0.43	0.89	25	3	0.1	Foam
D	30	0.43	0.89	25	3	0.1	Foam
E	10	0.43	0.89	15	3	0.1	Foam
F	10	0.43	0.89	37	3	0.1	Foam
G	10	1.20	0.89	25	3	0.1	Foam
H	10	0.43	0.89	25	9	0.2	Foam
I	10	0.43	0.89	25	3	0.2	Foam
J	0.5	0.01	0.89	25	3	0.1	Foam
K	0.5	0.01	0.89	25	1	—	Water

We varied the injection flowrate Q, the tube length ℓ and radius a, the initial volume V_0 of the foam-filled syringe, the viscosity μ of the liquid in the foam, and the liquid volume fraction ϵ_∞ of the foam.

observed $V(t)$ to be significantly different from that of incompressible flows. Since Q is constant, the nonlinear dependence of V on time (Fig. 2*B*) indicates that the foam is compressed throughout the experiment. The experimental results vary with Q, ℓ, a, and the initial volume of the syringe V_0. We also change the foam properties, in particular μ and ϵ_∞, by mixing glycerol and water with the foam. The effects of both μ and ϵ_∞ on the experimental results are negligible, as shown by experiments B, H, and I in Fig. 2*B*.

Below, we use physical arguments to identify the important dimensionless groups and rationalize our experimental observations. Assuming that ϵ is uniform throughout the syringe, liquid mass conservation requires that $\mathrm{d}[\epsilon(V_0 - Qt)]/\mathrm{d}t + \epsilon\pi a^2 u = 0$ at the tube inlet. The first term represents the rate of change in the mass of foam in the syringe due to the injection. The second term is the mass flow rate of foam vented into the tube. The first term gives a characteristic time of injection $t^* = V_0/Q$ over which relative changes of ϵ are of $\mathcal{O}(1)$. Then, liquid mass conservation inside the tube, $\partial\epsilon/\partial t + \partial(\epsilon u)/\partial z = 0$, establishes a characteristic foam speed $u^* = \ell/t^* = \ell Q/V_0$. The ratio between the characteristic foam speed u^* in the tube and the speed u_D, at which compressibility effects dominate (Eq. **1**), defines a dimensionless injection rate

$$\varphi \equiv \frac{u^*}{u_D} = \frac{Q\gamma\mu\kappa^2\ell^3}{V_0(\bar{R}ap_\infty)^2}. \qquad [2]$$

The dimensionless parameter φ is also a measure of the magnitude of the pressure drop Δp_t along the tube relative to atmospheric pressure p_∞. Combining Eqs. **1** and **2**, where the foam velocity in the tube is $u = \mathcal{O}(u^*)$, the dimensionless pressure drop along the tube is $\Delta p_t/p_\infty = \mathcal{O}(\sqrt{\varphi})$. Thus, a larger injection rate φ results in greater compressibility effects in the foam flow.

Fast-Injection Regime. The value of φ for each experiment is calculated and shown in Fig. 2*C*. For experiments A–I, $\varphi = \mathcal{O}(1)$ so that $\Delta p_t/p_\infty = \mathcal{O}(1)$. Therefore, the injection is fast enough so that compressibility effects are important and the experiments are in the fast-injection regime. The foam volume at the outlet $V(t) = \pi a^2 \int u\mathrm{d}t$ therefore has a characteristic scale $\pi a^2 u^* t^* = \pi a^2 \ell$, suggesting a dimensionless volume $\mathcal{V} = V/(\pi a^2 \ell)$. A dimensionless time τ can be defined as time rescaled with the characteristic injection time t^*—that is, $\tau \equiv (t - t_0)/t^*$. After nondimensionalizing our data in Fig. 2*B* using the dimensionless groups ($\mathcal{V}$ and τ) obtained above, we find that the dimensionless data of volume $\mathcal{V}$ and time τ collapse onto a universal curve over a range of injection rate Q, initial volume V_0, tube length ℓ and radius a, liquid viscosity μ, and liquid volume fraction ϵ_∞, as shown in Fig. 2*C*.

The dimensionless universal curve is well-fit by a power law at the late times, as shown by the solid line in Fig. 2*C*:

$$\mathcal{V} = \beta\tau^\alpha \quad \text{for} \quad \varphi = \mathcal{O}(1), \qquad [3]$$

where $\beta = 39 \pm 6$ and $\alpha = 2.5 \pm 0.3$ are dimensionless fitting parameters averaged over all fast-injection experiments. Near the end of some experiments ($\tau \approx 1$), the data deviate from the power law. Note that Eq. **3** shows no dependence of foam flow dynamics on μ and ϵ_∞, which agrees with the observations (experiments B and H). The experimental system contains 10 parameters ($Q, \ell, a, V_0, \mu, \gamma, \epsilon_\infty, \bar{R}, V, t$) yet can, for the parameter range of our experiments, be adequately described with a simple power law involving two dimensionless parameters ($\mathcal{V}$ and τ).

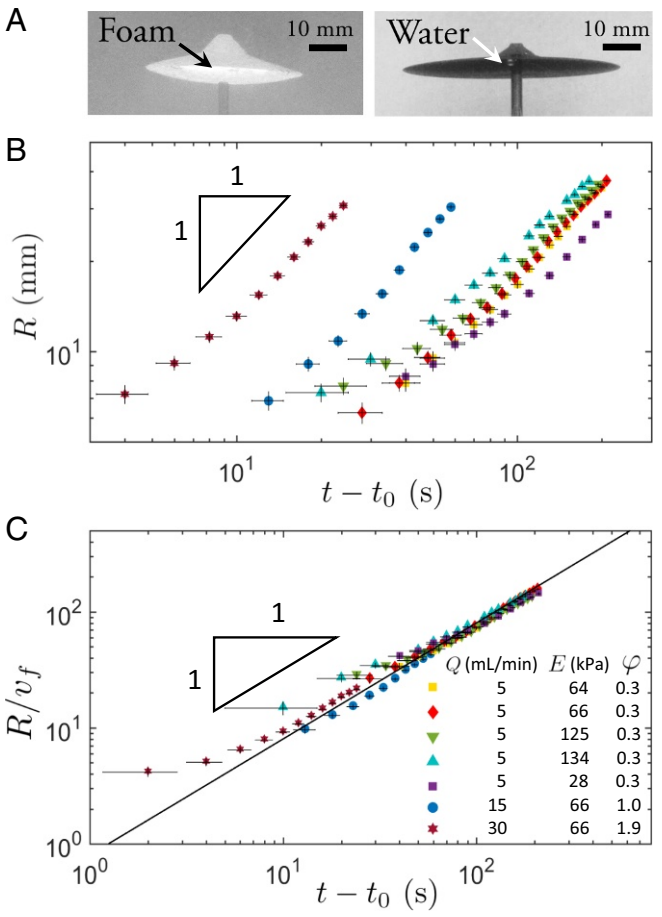

Fig. 3. (*A*) A snapshot of fracture driven by foam and water injection taken at $t - t_0 = 100$ s, where t_0 is the time when the fracture starts to grow. Although the experimental parameters are the same for both foam and water ($Q = 5$ mL/min and $E = 66$ kPa), the fracture size is visibly different. (*B*) The radius R of a foam-driven crack measured in time for the fast-injection regime [$\Delta p_t/p_\infty = \mathcal{O}(\sqrt{\varphi}) = \mathcal{O}(1)$]. Different curves correspond to experiments with different E and Q. The fracture radius grows linearly with time at the late times, which is different from the results of the incompressible fluid-driven cracks (see *SI Appendix*). (*C*) The collapse of data rescaled by Eq. **5** shows a good agreement between the experiments and the scaling law of fracture growth driven by compressible foam flow (the solid line). The dimensionless prefactor $A = 0.8 \pm 0.1$ is obtained by fitting Eq. **5** to each experimental curve at late times.

Slow-Injection Regime. On the other hand, when $\varphi \ll 1$, $\Delta p_t / p_\infty = \mathcal{O}(\sqrt{\varphi}) \ll 1$. Then, compressibility effects are small and the experiments are in the slow-injection regime. The flow approaches a steady state ($\partial\epsilon/\partial t = 0$) with $u = Q/(\pi a^2)$ and $V = Q(t - t_0)$ (see Expt. J where ℓ and Q are sufficiently small so that $\varphi \approx 4 \times 10^{-7}$). The injection of water (Expt. K, $t_0 = 0$) in comparison with foam (Expt. J, $t_0 = 80$ s) at the same Q, a, ℓ, V_0 is shown in Fig. 2*b*. The crossover time at which foam flow approaches the incompressible result $V = Q(t - t_0)$ (dashed line in Fig. 2*b*) can be estimated by matching the initial unsteady velocity with the incompressible steady-state asymptote. At short times, the mass flux vented into the tube is small, so that the pressure increase δp_s and volume decrease $-\delta V_s$ in the syringe for isothermal compression follows $\delta p_s / p_\infty \approx -\delta V_s / V_0 \approx Qt/V_0 = \tau$. The initial unsteady foam flow velocity (Eq. **1**) is $u \approx u_D (\delta p / p_\infty)^2 \approx u_D \tau^2$ and volume is $V \approx \frac{\pi}{3} a^2 u_D t^* \tau^3$. The time for foam to reach the steady-state result $Q(t - t_0) = Q\tau t^*$ is therefore $\tau_c = \sqrt{3\varphi V_0/(\pi a^2 \ell)}$. For Expt. J in Fig. 2 the crossover time is $t_c - t_0 = \sqrt{\varphi V_0^3/(\pi a^2 \ell Q^2)} \approx 100$ s, which gives an order-of-magnitude estimate of the time when $V(t)$ approaches the incompressible limit. Note that although the fast-injection experimental results (Fig. 2*c*) are independent of μ, the crossover time t_c for the slow-injection experiment depends on φ and thus is affected by the foam properties.

A Quantitative Description for Foam-Driven Fractures

We can now apply our findings for $\mathcal{V}(\tau)$ from the one-dimensional experiments to foam-driven fractures in elastic solids (Fig. 1). We conduct fracturing experiments with $Q = 5{-}30$ mL/min, $E = 28{-}125$ kPa, and $\varphi = \mathcal{O}(1)$ and, in each case, measure the radius of the lens-shaped crack $R(t)$ (Fig. 1*D*) as a function of time, as plotted in Fig. 3*B*. We observe a linear increase of crack radius $R(t)$ with time, which differs from the crack growth driven by incompressible flows (see *SI Appendix*).

For a lens-shaped fracture of radius R inside an elastic medium with energy per unit area required to open new crack surfaces $2\gamma_s$ (48, 49), the elastic stress around the fracture is $\Delta p_e \approx EW/(2(1-\sigma^2)R)$ (37, 46, 47), and the pressure required to break the atomic/molecular bonds and extend the fracture is $\Delta p_f \approx \sqrt{\pi\gamma_s E/(2R)}$ (47–51). Assuming the stored elastic energy in the solid matrix is instantaneously dissipated by creating new crack surfaces (31, 38, 48, 51), according to $\Delta p_e \approx \Delta p_f$, we find

$$\frac{E}{2(1-\sigma^2)}\frac{W}{R} \approx \sqrt{\frac{\pi\gamma_s E}{2R}}. \qquad [4]$$

For all of our experiments, the viscous stresses along the tube Δp_t are large compared with Δp_e and Δp_f. However, the viscous stresses Δp_v due to flow within the fracture are negligible since $\Delta p_v \ll \Delta p_f$, as shown in *SI Appendix*. In addition, the foam-driven fractures are designed to grow horizontally so that the buoyancy due to the density difference between foam and gelatin does not affect the fracture dynamics.

We recall that the volumetric flux of foam in the tube is determined by the pressure drop along the tube Δp_t rather than the stresses related to fracture formation Δp_e since $\Delta p_e \ll \Delta p_t$. Thus, the volume of foam V vented into the fracture at the outlet of the needle obeys the same power law as the volume collected at the tube outlet in the one-dimensional model experiments (Fig. 2 and Eq. **3**). Since $\varphi = \mathcal{O}(1)$ in the fracture experiments, we use the volumetric flux in the fast-injection regime—that is, $\mathcal{V} = \beta\tau^\alpha$. Combining Eqs. **3** and **4**, the experimental value $\alpha = 2.5$ (Fig. 2*C*), and the crack volume $V = 4\pi/3\, WR^2$ for an elliptical fracture, we obtain

$$R = Av_f(t - t_0), \quad v_f \equiv \left(\frac{9\beta^2 a^4 \ell^2 E}{32\pi(1-\sigma^2)^2\gamma_s}\right)^{1/5}\frac{Q}{V_0}, \qquad [5]$$

where A is a dimensionless numerical prefactor that depends only on the shape of the fracture and t_0 is the time when foam first enters the gelatin matrix. The collapse of the rescaled experimental data (symbols) at the late times in Fig. 3*C* shows excellent agreement with the prediction for fracture dynamics given by Eq. **5** (Fig. 3*C*, solid line). Note that the speed of crack propagation v_f for foam injection is constant, in contrast with incompressible fluid-driven fractures where the fracturing velocity decreases with time.

Although foam consists of water and gas, the dynamics of foam-driven fractures for $\varphi = \mathcal{O}(1)$, where the compressibility of foam is important, differs significantly from those of fractures driven by the injection of either water or gas. Water is effectively incompressible, so $V = Qt$. Gas is compressible but has a small resistance to flow in the tube, and so the pressure drop is not large enough to probe compressibility effects. Foam is as compressible as gas but has a large viscous resistance to flow along the tube. This produces a large pressure drop in the tube, $\Delta p_t \geq p_\infty$, causing compression. We checked the foam-fracture experiments in the slow-injection regime ($\varphi \ll 1$) where compressibility effects are small. The dynamics of fracture growth driven by slow injection of foam obeys the same scaling law as the classical results of crack growth driven by incompressible flows, $R(t) \approx (9Q^2E/(32\pi^3(1-\sigma^2)^2\gamma_s))^{1/5} t^{2/5}$, as shown in *SI Appendix*.

Conclusion

In conclusion, we study the flow of compressible foam through a tube and its impact on fractures in elastic solids driven by foam injection. We found two flow regimes depending on whether or not the injection is fast enough to cause significant compression of the foam. In the fast-injection regime, a time-dependent flow was observed as a result of compressed bubbles in the foam. In the slow-injection regime, the flow approaches the incompressible results within the experimental timescale. Finally, we demonstrated that a scaling argument based on our empirical result of the mass balance of foam flow and the stress balance for fracture propagation exhibits excellent agreement with our experiments of foam-driven fractures. Our results could potentially inform other systems involving injection of compressible two-phase flows in channels with narrow geometries.

ACKNOWLEDGMENTS. We thank Sascha Hilgenfeldt and Allan Rubin for helpful discussions. We acknowledge funding from National Science Foundation Grant CBET-1509347. C.-Y.L. thanks the Princeton Environmental Institute for funding via the Mary and Randall Hack '69 Graduate Fund and the Andlinger Center for Energy and the Environment for the Maeder Graduate Fellowship. B.R. acknowledges partial support from the Carbon Mitigation Initiative of Princeton University.

1. Figueredo RCR, Sabadini E (2003) Firefighting foam stability: The effect of the drag reducer poly (ethylene) oxide. *Coll Surf A* 215:77–86.
2. Magrabi SA, Dlugogorski BZ, Jameson GJ (2002) A comparative study of drainage characteristics in afff and fffp compressed-air fire-fighting foams. *Fire Saf J* 37:21–52.
3. Gardiner BS, Dlugogorski BZ, Jameson GJ (1998) Rheology of fire-fighting foams. *Fire Saf J* 31:61–75.
4. McBride TO, et al. (2014) US Patent 8,806,866 B2. Systems and Methods for Foam-Based Heat Exchange During Energy Storage and Recovery Using Compressed Gas 19.
5. Klempner D, Frisch KC (1991) *Handbook of Polymeric Foams and Foam Technology* (Hanser, Munich), Vol 404.
6. Lv Q, et al. (2017) Wall slipping behavior of foam with nanoparticle-armored bubbles and its flow resistance factor in cracks. *Sci Rep* 7:5063.
7. Sun Q, et al. (2015) Properties of multi-phase foam and its flow behavior in porous media. *RSC Adv* 5:67676–67689.
8. Worthen AJ, et al. (2014) Carbon dioxide-in-water foams stabilized with a mixture of nanoparticles and surfactant for CO2 storage and utilization applications. *Energy Proced* 63:7929–7938.

9. Aronson AS, Bergeron V, Fagan ME, Radke CJ (1994) The influence of disjoining pressure on foam stability and flow in porous media. *Coll Surf A* 83:109–120.
10. Hirasaki GJ, Lawson JB (1985) Mechanisms of foam flow in porous media: Apparent viscosity in smooth capillaries. *Soc Petro Eng J* 25:176–190.
11. Géraud B, Jones SA, Cantat I, Dollet B, Méheust Y (2016) The flow of a foam in a two-dimensional porous medium. *Water Resour Res* 52:773–790.
12. Bergeron V, Fagan ME, Radke CJ (1993) Generalized entering coefficients: A criterion for foam stability against oil in porous media. *Langmuir* 9:1704–1713.
13. Environmental Protection Agency (2016) Hydraulic Fracturing for Oil and Gas: Impacts from the Hydraulic Fracturing Water Cycle on Drinking Water Resources in the United States (US Environmental Protection Agency, Washington, DC), EPA/600/R-16/236F.
14. Barbati AC, Desroches J, Robisson A, McKinley GH (2016) Complex fluids and hydraulic fracturing. *Annu Rev Chem Biomol Eng* 7:415–453.
15. Mack DJ, Harrington LJ (1990) New foams introduce new variables to fracturing. *Oil Gas J* 88:49–58.
16. Bullen RS, Bratrud TF (1976) Fracturing with foam. *J Can Pet Technol* 15:27–32.
17. Wanniarachchi WAM, et al. (2015) Current opinions on foam-based hydro-fracturing in deep geological reservoirs. *Geomech Geophys Geo-energ Geo-resour* 1:121–134.
18. Enzendorfer C, et al. (1995) Pipe viscometry of foams. *J Rheol* 39:345–358.
19. Valko P, Economides MJ (1992) Volume equalized constitutive equations for foamed polymer solutions. *J Rheol* 36:1033–1055.
20. Gardiner BS, Dlugogorski BZ, Jameson GJ (1999) Prediction of pressure losses in pipe flow of aqueous foams. *Ind Eng Chem Res* 38:1099–1106.
21. Cantat I, Kern N, Delannay R (2004) Dissipation in foam flowing through narrow channels. *Europhys Lett* 65:726–732.
22. Terriac E, Etrillard J, Cantat I (2006) Viscous force exerted on a foam at a solid boundary: Influence of the liquid fraction and of the bubble size. *Europhys Lett* 74:909–915.
23. Lindner A, Coussot P, Bonn D (2000) Viscous fingering in a yield stress fluid. *Phys Rev Lett* 85:314–317.
24. Hubbert MK, Willis DG (1957) *Mechanics of hydraulic fracturing*. Petrol Trans 210:239–257.
25. Kavanagh JL, Menand T, Sparks RSJ (2006) An experimental investigation of sill formation and propagation in layered elastic media. *Earth Planet Sci Lett* 245:799–813.
26. Menand T, Tait SR (2002) The propagation of a buoyant liquid-filled fissure from a source under constant pressure: An experimental approach. *J Geophys Res Solid Earth* 107:2306.
27. Takada A (1990) Experimental study on propagation of liquid-filled crack in gelatin: Shape and velocity in hydrostatic stress condition. *J Geophys Res* 90:8471–8481.
28. Kavanagh JL, Menand T, Daniels KA (2013) Gelatine as a crustal analogue: Determining elastic properties for modelling magmatic intrusions. *Tectonophysics* 582:101–111.
29. Di Giuseppe E, Funiciello F, Corbi F, Ranalli G, Mojoli G (2009) Gelatins as rock analogs: A systematic study of their rheological and physical properties. *Tectonophysics* 473:391–403.
30. Lai CY, Zheng Z, Dressaire E, Wexler JS, Stone HA (2015) Experimental study on penny-shaped fluid-driven cracks in an elastic matrix. *Proc R Soc A* 471:20150255.
31. Lai CY, Zheng Z, Dressaire E, Stone HA (2016) Fluid-driven cracks in an elastic matrix in the toughness-dominated limit. *Phil Trans R Soc A* 374:20150425.
32. Lai CY, et al. (2016) Elastic relaxation of fluid-driven cracks and the resulting backflow. *Phys Rev Lett* 117:268001.
33. Ovarlez G, Krishan K, Cohen-Addad S (2010) Investigation of shear banding in three-dimensional foams. *Europhys Lett* 91:68005.
34. Durian DJ, Weitz DA, Pine DJ (1991) Scaling behavior in shaving cream. *Phys Rev A* 44:R7902–R7905.
35. Höhler R, Cohen-Addad S (2005) Rheology of liquid foam. *J Phys Condens Matter* 17:R1041.
36. Cohen-Addad S, Höhler R, Pitois O (2013) Flow in foams and flowing foams. *Annu Rev Fluid Mech* 45:241–267.
37. Spence DA, Sharp P (1819) Self-similar solutions for elastohydrodynamic cavity flow. *Proc R Soc A* 400:289–313.
38. Detournay E (2016) Mechanics of hydraulic fractures. *Annu Rev Fluid Mech* 48:311–339.
39. Denkov ND, Tcholakova S, Golemanov K, Subramanian V, Lips A (2006) Foam–wall friction: Effect of air volume fraction for tangentially immobile bubble surface. *Coll Surf A* 282:329–347.
40. Princen HM (1986) Osmotic pressure of foams and highly concentrated emulsions. I. Theoretical considerations. *Langmuir* 2:519–524.
41. Denkov ND, Subramanian V, Gurovich D, Lips A (2005) Wall slip and viscous dissipation in sheared foams: Effect of surface mobility. *Coll Surf A* 263:129–145.
42. Princen HM, Kiss AD (1987) Osmotic pressure of foams and highly concentrated emulsions. 2. Determination from the variation in volume fraction with height in an equilibrated column. *Langmuir* 3:36–41.
43. Koehler SA, Hilgenfeldt S, Stone HA (2000) A generalized view of foam drainage: Experiment and theory. *Langmuir* 16:6327–6341.
44. Koehler SA, Hilgenfeldt S, Stone HA (1999) Liquid flow through aqueous foams: The node-dominated foam drainage equation. *Phys Rev Lett* 82:4232.
45. Stone HA, Koehler SA, Hilgenfeldt S, Durand M (2003) Perspectives on foam drainage and the influence of interfacial rheology. *J Phys: Condens Matter* 15:S283–S290.
46. Sneddon IN (1946) The distribution of stress in the neighbourhood of a crack in an elastic solid. *Proc R Soc A* 187:229–260.
47. Lister JR, Kerr RC (1991) Fluid-mechanical models of crack propagation and their application to magma transport in dykes. *J Geophys Res* 96:10049–10077.
48. Griffith AA (1921) The phenomena of rupture and flow in solids. *Phil Trans R Soc A* 221:163–198.
49. Irwin GR (1957) Analysis of stresses and strains near the end of a crack traversing a plate. *J Appl Mech* 24:361–364.
50. Rice JR (1968) *Mathematical analysis in the mechanics of fracture. Fracture: An Advanced Treatise*, ed Liebowitz H (Academic, New York), Vol 2, pp 191–311.
51. Savitski AA, Detournay E (2002) Propagation of a penny-shaped fluid-driven fracture in an impermeable rock: Asymptotic solutions. *Int J Sol Struct* 39:6311–6337.